

Excitation of extraordinary modes inside the source of Saturn's kilometric radiation

Hao Ning^{1,2}, Yao Chen^{1,2}, Chuanyang Li^{1,2}, Shengyi Ye³, Alexey Kuznetsov⁴, and
Siyuan Wu³

¹ Institute of Frontier and Interdisciplinary Science, Shandong University, Qingdao, Shandong, 266237, People's Republic of China

e-mail: yaochen@sdu.edu.cn

² Institute of Space Sciences, Shandong University, Shandong, 264209, People's Republic of China

³ Department of Earth and Space Sciences, Southern University of Science and Technology, Shenzhen, Guangdong, People's Republic of China

⁴ Institute of Solar-Terrestrial Physics, Irkutsk, 664033, Russia

Received ; accepted

ABSTRACT

The electron cyclotron maser instability (ECMI) of extraordinary mode waves was investigated with the parameters observed in Saturn's kilometric radiation (SKR) sources. Previous studies employed simplified dispersion relations, and did not consider the excitation of the relativistic (R) mode. This mode is introduced by considering the relativistic effect in plasmas consisting of both cold and hot electrons. Using particle-in-cell simulations, we investigated the excitation of R and X modes based on the measured data. Using the reported value of the density ratio of energetic to total electrons $n_e/n_0 = 24\%$, the most unstable mode is the R mode. The escaping X-mode emissions are amplified only if the energetic electrons are dominant with $n_e/n_0 \geq 90\%$. For these cases, only the X mode is excited and the R mode disappears due to its strong coupling. The results are well in line with the linear kinetic theory of ECMI. The properties of both the R and X modes are consistent with the observed SKR emissions. This raises questions about the nature of the measured electric field fluctuations within "presumed" SKR sources. The study provides new insights into the ECMI process relevant to SKR emission mechanisms.

Key words. Planets and satellites: gaseous planets – Radio continuum: planetary systems – Masers – Waves – Plasmas – Methods: numerical

1. Introduction

Saturn's kilometric radiations (SKRs) represent intense radio emissions originating from the Kronian auroral region, considered to be the counterpart of the auroral kilometric radiations (AKRs) on Earth (see, e.g., Kaiser et al. 1980, 1981; Gurnett et al. 2004; Kurth et al. 2005; Lamy et al. 2009). The radiations are observed in the kilohertz to megahertz frequency range, and the radiated powers of 10^8 – 10^{10} watts. Furthermore, SKRs are closely related to Saturn's magnetosphere dynamics (Jackman 2011; Kimura et al. 2013), and have been extensively studied.

Saturn's kilometric radiations are often strongly polarized with narrow beaming angles and high intensity (Lamy et al. 2008, 2018), indicating coherent emissions generated by electron cyclotron maser instability (ECMI) (Wu & Lee 1979; Wu 1985; Treumann 2006; Bingham et al. 2013). The instability excites escaping modes at gyro-frequencies ($\sim \Omega_{ce}$) via a gyro-resonant wave-particle interaction, driven by electrons with anisotropic velocity distribution functions (VDFs; see Ning et al. 2021a,b, for recent studies). The ECMI is now widely applied to planetary and stellar radio emissions.

The Cassini spacecraft measures the radio waves with the Radio and Plasma Wave Science (RPWS, Gurnett et al. 2004) instrument and the electrons with the Cassini Plasma Spectrometer Electron Spectrometer (CAPS/ELS, Linder et al. 1998; Young et al. 2004) in Saturn's magnetosphere. Since 2010, researchers have reported several crossings of SKR sources by Cassini, identified with the cutoff frequency of the spectrum close to or slightly lower than the local Ω_{ce} (e.g., Kurth et al. 2011; Mutel et al. 2010; Lamy et al. 2010; Menietti et al. 2011; Lamy et al. 2018).

As has previously been reported, SKR sources are characterized by a low ratio of plasma oscillation frequency to electron gyro-frequency ($\omega_{pe}/\Omega_{ce} < 0.1$), in accordance with the ECMI conditions ($\omega_{pe}/\Omega_{ce} < 1$, Wu & Lee 1979). The emissions mainly propagate quasi-perpendicularly to the background magnetic field with linear polarization near the sources, consistent with the X-mode properties. The energy conversion rate from electrons to radiations is $\sim 1\%$ (Lamy et al. 2011). The abundances of energetic and cold electrons are comparable with each other (Schippers et al. 2011).

The measurement of electron VDFs is crucial to the study of the ECMI process. In the first encounter of the SKR source by Cassini in 2008, Mutel et al. (2010) found that the cold and hot electrons can be fitted with a Kappa and a Dory-Guest-Harri (DGH, Dory et al. 1965) distribution, respectively. They further calculated the corresponding ECMI growth rates of X-mode emissions with the linear kinetic theory, and suggested that the ECMI process can efficiently amplify this escaping X mode below Ω_{ce} , along directions perpendicular to the magnetic field. Menietti et al. (2011) investigated the ECMI process of another SKR source using a similar method and obtained the same results. They also suggested that O-mode and Z-mode waves can be generated.

However, these studies on the ECMI of SKRs followed Mutel et al. (2007) and employed the dispersion relations of pure relativistic energetic electrons. They estimated the correction to the dispersion relation with a scale factor when calculating the growth rates of the X and Z modes,

rather than solving the dispersion matrix to calculate the real frequency and the growth rate in a self-consistent manner. As reported by Mutel et al. (2010) and Menietti et al. (2011), the density ratio of the energetic to the total electrons was fitted as $n_e/n_0 = 20\%–24\%$. With this range of n_e/n_0 (and other comparable values), one obtains very different dispersion relations. For waves perpendicular to the magnetic field, the gyro-resonance condition is simplified as $\omega = n\Omega_{ce}/\gamma < n\Omega_{ce}$. When adopting the cold-plasma dispersion relation deduced from the magneto-ionic theory, the ECMI process cannot amplify the fundamental X mode with the cutoff frequency (ω_X) being larger than Ω_{ce} . For pure energetic electrons, the X-mode cutoff is less than Ω_{ce} and thus can grow via ECMI (e.g., Winglee 1983; Pritchett 1984a; Winglee 1985; Robinson 1986).

For plasmas consisting of both the cold and energetic electrons, another important mode may emerge. This mode, first deduced by Pritchett (1984b), appears in the range of $\Omega_{ce}/\gamma < \omega < \Omega_{ce}$. It is relevant to the relativistic effect, and is therefore called the relativistic (R) mode (Strangeway 1985, 1986). Our present study shows that the R mode becomes the most unstable mode, and is probably relevant to SKR. However, it is trapped and cannot escape. This mode has not been considered in studies on SKR sources, to the best of our knowledge.

According to the earlier reports on the crossings of SKR sources by Cassini, both cold and hot components of electrons exist with comparable densities (Schippers et al. 2011). This raises questions concerning the applicability of the oversimplified dispersion relations adopted by Mutel et al. (2010) and Menietti et al. (2011), which did not consider the existence of the R mode. For this study, we conducted fully kinetic electromagnetic particle-in-cell (PIC) simulations with the electron VDFs and plasma parameters reported by Menietti et al. (2011) to investigate the extraordinary modes (including R, X, and Z) and their coupling within SKR sources. We conducted a parametric study on n_e/n_0 , and applied the kinetic linear theory to verify and explain the PIC simulations.

2. Numerical method and parameter setting

As reported by Menietti et al. (2011), the frequency ratio was $\omega_{pe}/\Omega_{ce} = 0.046$, and the VDFs of both the cold and hot electrons were written as

$$f_0 = \frac{1}{(2\pi)^{3/2}v_0^3} \exp\left(-\frac{u^2}{2v_0^2}\right) \quad (1)$$

and

$$f_e = \frac{1}{j!(2\pi)^3/2v_\perp^2v_\parallel} \left(\frac{u_\perp^2}{2v_\perp^2}\right)^j \exp\left(-\frac{u_\perp^2}{2v_\perp^2} - \frac{u_\parallel^2}{2v_\parallel^2}\right), \quad (2)$$

respectively, where $j = 11$, u represents the momentum per mass, and v_\parallel ($= 0.11c$) and v_\perp ($= 0.038c$) represent the thermal velocity of the DGH distribution along parallel and perpendicular directions. The density ratio of the energetic to the total electrons was fitted to be $n_e/n_0 = 24\%$. Considering the uncertainties of the source measurements, we conducted a parametric study of n_e/n_0 . The models and parameter settings are presented below.

2.1. PIC simulations

We employed the Vector-PIC (vPIC) code developed by the Los Alamos National Laboratory (LANL). The code employs a second-order, explicit, leapfrog algorithm to update the positions and the velocities of charged particles, along with a full Maxwell description of the electric and magnetic fields via a second-order finite-difference time-domain solver (Bowers et al. 2008, 2009).

We performed 2D3V (two spatial dimensions with three velocity components) simulations in the xOz plane with periodical boundary conditions and a uniform background magnetic field ($\mathbf{B}_0 = B_0 \hat{e}_z$). The simulation domain was set to $L_x = L_z = 2048\Delta$, the grid length to $\Delta = 0.019 \lambda_{DE}$, and the time step to $\Delta t = 0.0097 \omega_{pe}^{-1}$.

Two components of electrons were included. Their distribution functions are described by Eqs. (1) and (2), and the center of the VDF of energetic electrons is at $v_\perp \sim 0.18 c$ (Fig. 1(a)). The thermal velocity of the low-energy electrons was set to $v_0 = 0.01c$ (~ 50 eV). The charge neutrality was maintained by including thermal protons with a realistic proton-to-electron mass ratio of 1836 and the same temperature (with the thermal velocity $v_p = v_0 / \sqrt{1836}$). We included 1000 macroparticles per cell for each component of the electrons and 500 for the protons.

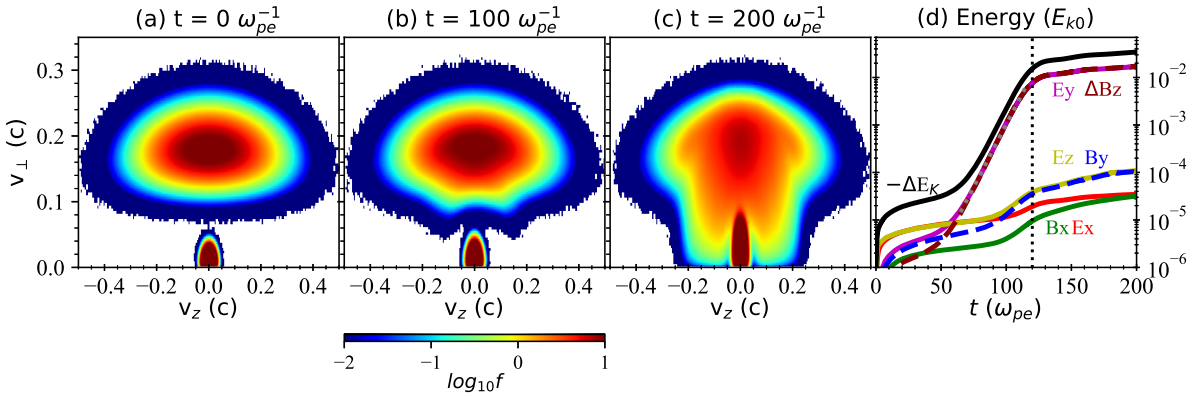


Fig. 1. Evolution of electron VDFs and energy profiles of the simulation with $n_e/n_0 = 24\%$. Panels (a–c): Snapshots of the VDFs at the start (a, $t = 0 \omega_{pe}^{-1}$), middle (b, $100 \omega_{pe}^{-1}$), and end (c, $200 \omega_{pe}^{-1}$) of the simulation. Panel (d): Temporal variations of energies of the six fluctuated field components. The black line represents the decline of the electron kinetic energy ($-\Delta E_k$). The energies are normalized to the initial kinetic energy of the total electrons. The gray dashed line represents the exponential fitting of the energy profiles. The vertical dotted line in (d) indicates the separate time ($120 \omega_{pe}^{-1}$) of the linear stage and the saturation stage.

2.2. Linear analysis of ECMI

Following the analysis of Pritchett (1984b), we employed the δ function below to describe the two components of electrons,

$$f = \left(1 - \frac{n_e}{n_0}\right) \delta(u_\perp) \delta(u_\parallel) + \frac{n_e}{n_0} \delta(u_\perp - u_r) \delta(u_\parallel), \quad (3)$$

where u_r refers to the momentum of the energetic electrons. In accordance with the PIC simulation, we assumed the waves propagate in the xOz plane with $\mathbf{B}_0 = B_z \hat{e}_z$. For simplicity, only the perpendicular propagating waves with $k_\parallel = 0$ were studied.

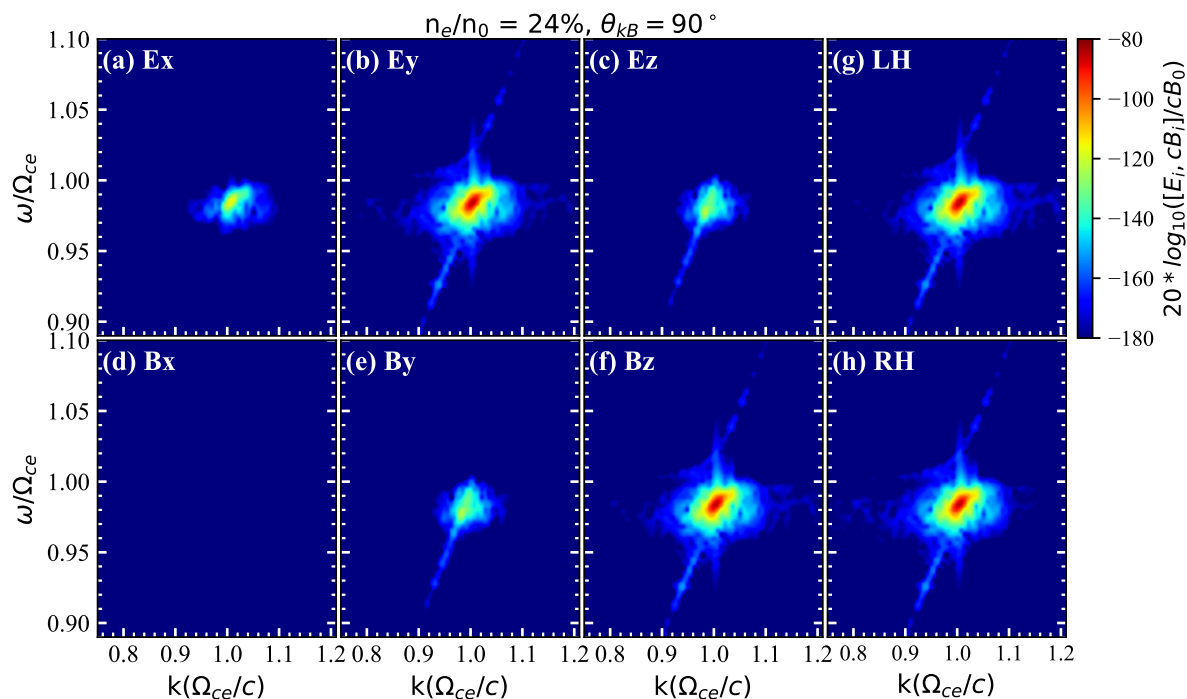


Fig. 2. Wave dispersion diagrams of electric and magnetic fields with $n_e/n_0 = 24\%$ and $\theta_{kB} = 90^\circ$, during the interval of $[100, 200] \omega_{pe}^{-1}$. The six field components are provided in panels (a–f) and the separated LH and RH components in panels (g–h).

With the VDF presented above, we derived the elements of the plasma dispersion tensor (Eq. (A.1)) and obtained the frequencies and the growth rates of the ECMI modes by numerically solving their determinant. We analyzed the dispersion relations, the ECMI growth rates, and the polarization of the X and R modes. The results are presented in the appendix.

3. PIC simulations

We present the PIC simulations with the reported SKR source parameters as the reference case with ($n_e/n_0 = 24\%$) to show the excitation and properties of extraordinary modes (R, X, Z), followed by the parametric study on n_e/n_0 to explore its effect.

3.1. Results with measured parameters ($n_e/n_0 = 0.24$)

According to the energy profiles presented in Fig. 1(d), the wave excitation and further evolution can be divided into two stages, the linear ($0\text{--}120 \omega_{pe}^{-1}$) stage and the saturation ($120\text{--}200 \omega_{pe}^{-1}$) stage. In the linear stage, the energies of $\Delta B_z (= B_z - B_0)$ and E_y rise rapidly, reaching the level of $10^{-2} E_{k0}$ (E_{k0} is the initial kinetic energy of total electrons). The electron kinetic energy (E_k) declines in accordance with the growth of the ECMI modes. The energies of other field components are much weaker, being $\sim 10^{-5} E_{k0}$. In the saturation stage, the energies of all the fields rise gradually. In total, $\sim 3.4\%$ of E_{k0} was converted to wave energies.

Figure 1(a–c) presents the evolution of the electron VDFs. The two components are initially separated. Within $100\text{--}200 \omega_{pe}^{-1}$, the shell-like hot electrons diffuse in the phase space, later de-

veloping a butterfly-like morphology. Meanwhile, the cool Maxwellian electrons are significantly energized along the perpendicular direction.

We performed a fast Fourier transform (FFT) analysis on each field component. In Fig. 2(a–f), we show the $\omega - k$ dispersion diagrams for perpendicular-propagating waves with $\theta_{kB} = 90^\circ$ (the angle between \mathbf{k} and \mathbf{B}_0), along which the ECMI waves are the most amplified. The strongest wave appears in the E_y and B_z components, with frequencies of $\sim 0.98 \Omega_{ce}$, in accordance with the dispersion relation of the R mode as shown in the Appendix. This mode can be identified as the transverse electromagnetic wave with significant E_y and B_z components and an insignificant E_x component. The property of the simulated R mode is in line with the linear kinetic theory (see Section A.2).

To separate the left-hand (LH) and right-hand (RH) polarized components of the R mode, we processed (E_x, E_y) with the following equation:

$$E_{LH,RH} = \frac{1}{\sqrt{2}}(E_x \pm iE_y). \quad (4)$$

The results are presented in Fig. 2(g–h). The intensities of the LH and RH components are comparable to each other, indicating a strong linear polarization.

According to the energy profiles in Fig. 1(d), the total energy of the R mode is $\sim 0.034 E_{k0}$, and its growth rate can be fitted as $\Gamma = 5.57 \times 10^{-3} \Omega_{ce}$. The fundamental O mode is slightly amplified in E_z and B_y . Its total energy is weaker than the R mode by approximately two orders of magnitude.

In this case, only the R mode can be amplified, with no significant growth of X. The results can be clearly understood with the linear kinetic theory. As shown in the Appendix, the R mode is the most unstable at $k \sim \Omega_{ce}/c$ with a maximal growth rate of $0.006 \Omega_{ce}$, and linearly polarized in E_y with $E_x/iE_y \sim 0$ (Fig. A.1(a–c)). The growth rates of the X mode remain at 0 with its cutoff being larger than Ω_{ce} .

3.2. Effect of n_e/n_0

Considering the uncertainties of the electron measurement of Cassini CAPS/ELS, we varied the values of n_e/n_0 from 10% to 100% to investigate the conditions for X-mode excitations. For cases with a $n_e/n_0 > 10\%$, the simulations lasted for $200 \omega_{pe}^{-1}$, and for the $n_e/n_0 = 10\%$ case, the simulation lasted for $300 \omega_{pe}^{-1}$.

In Fig. 3(a–e), we plotted the energy profiles of each case. As introduced in Section 3.1, we divided the whole ECMI process into two stages, the linear stage and the saturation stage. For each case we observed a sharp rise of E_y in the linear stage. The energy conversion rates from the electron kinetic energy to the waves is $\sim 10^{-2}$. With a higher n_e/n_0 , the wave excitation is more impulsive, with a short linear stage. For cases with $n_e/n_0 \geq 50\%$, we observed a gradual decline of the field energies and $-\Delta E_k (= E_{k0} - E_k)$, suggesting further damping of the amplified waves. Figure 4 displays the evolution of the VDFs in different cases. With a larger n_e/n_0 , the VDF of the

hot electrons diffuses faster, and the cold electrons are more efficiently accelerated. The VDFs do not change much after $50\text{--}100 \omega_{pe}^{-1}$.

For each case, we performed a FFT analysis of the fluctuated fields to show the amplified wave modes (Fig. 5). The waves in E_x and E_z are not shown here since they are very weak. For cases with $n_e/n_0 \leq 70\%$, the R mode is the most intensive, while no significant X mode appears. With increasing n_e/n_0 , the R-mode dispersion curve becomes flatter and closer to that of the X mode. With $n_e/n_0 \geq 90\%$, the two dispersion curves merge, indicating their strong coupling; this leads to the significant excitation of the X mode with a lower cutoff frequency of $\omega_X \sim 0.97 \Omega_{ce}$.

We plotted the growth rates (Γ) of the simulated R mode (or the X mode for the cases with $n_e/n_0 = 90$ and 100%) by fitting the energy curves (Fig. 3(f)). The values of Γ rise from 0.0032 to $0.018 \Omega_{ce}$ with n_e/n_0 from 10% to 100% . With the linear kinetic theory (see Fig. A.2 of the Appendix), we obtained comparable growth rates for the R (for the cases with $0 < n_e/n_0 < 100\%$) and the X mode (for the case with $n_e/n_0 = 100\%$), which rise from 4.59×10^{-3} to $1.14 \times 10^{-2} \Omega_{ce}$.

According to our PIC simulations, the X mode is excited only if the energetic component is dominant ($n_e/n_0 \geq 90\%$). The characteristics of the X mode in the case of $n_e/n_0 = 100\%$, including the growth rate, polarization, and wave fields (see Figs. 3(e), 4(e), and 6), are consistent with the linear kinetic theory (Fig. A.1(d–f)). In this case, the X mode becomes saturated within the first $50 \omega_{pe}^{-1}$, mainly in E_y and B_z , and much less so in E_x . The energy conversion rate from energetic electrons to the X mode is $\sim 3\%$, and the growth rate is $\sim 0.018 \Omega_{ce}$, similar to that obtained by

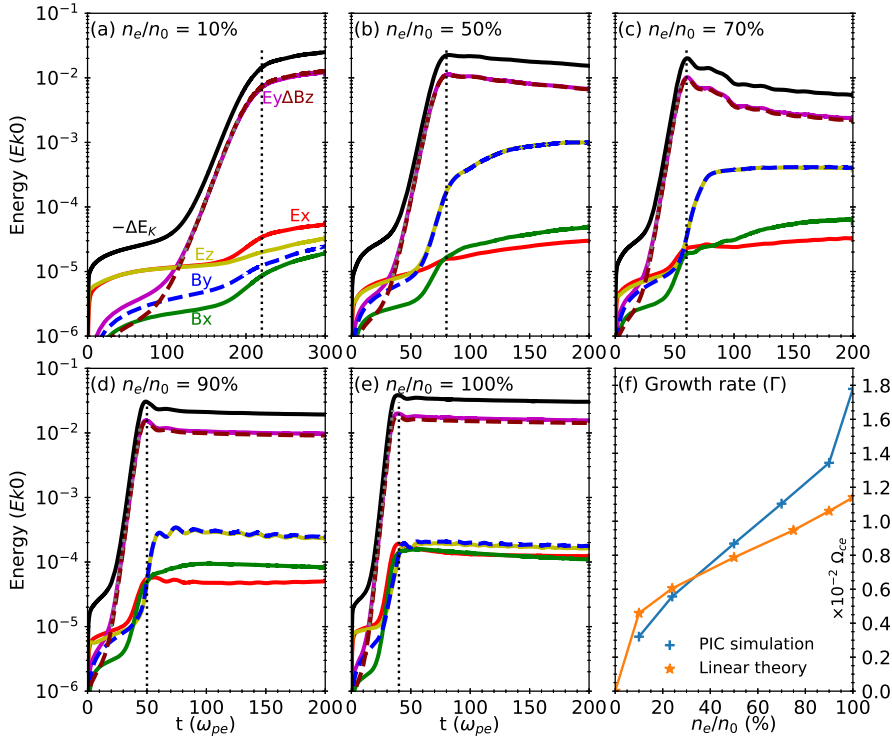


Fig. 3. Energy profiles and growth rates for different simulation cases. Panels (a–e): Energy profiles of the six fluctuated field components for the cases with $n_e/n_0 = 0.1, 0.5, 0.7, 0.9$, and 1.0 . The energies are normalized to the respective initial kinetic energy of total electrons of each case. Panel (f) presents the growth rates with different density ratios obtained by the PIC simulations (blue) and the linear kinetic theory (orange).

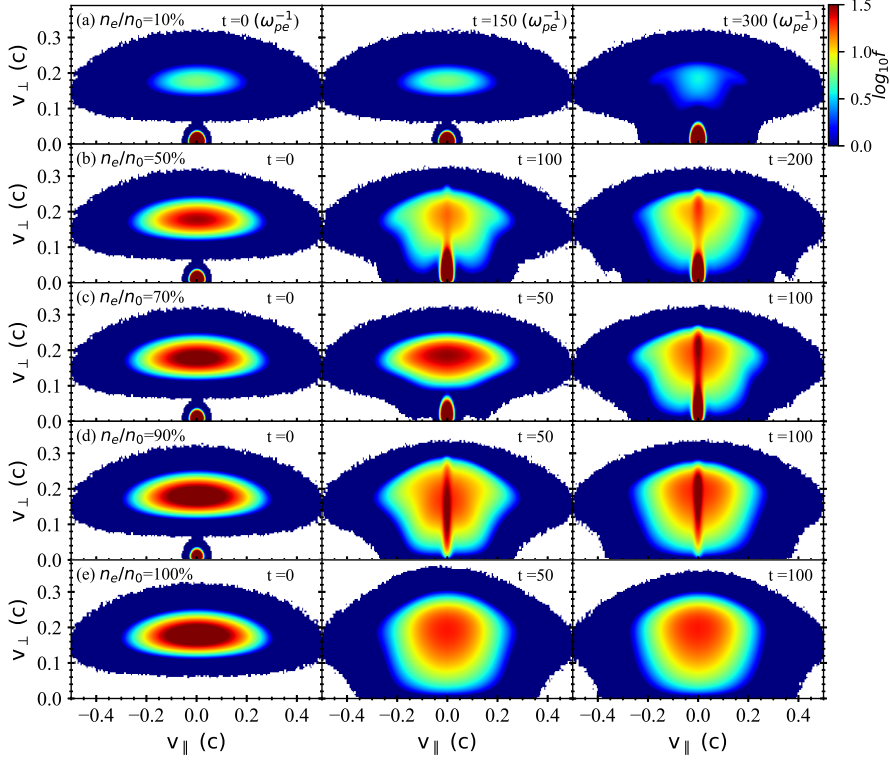


Fig. 4. Snapshots of VDFs of simulations with $n_e/n_0 = 10\%$ (a), 50% (b), 70% (c), 90% (d), and 100% (e) at moments representative of the initial (left), the transition (middle), and the saturation (right) stages.

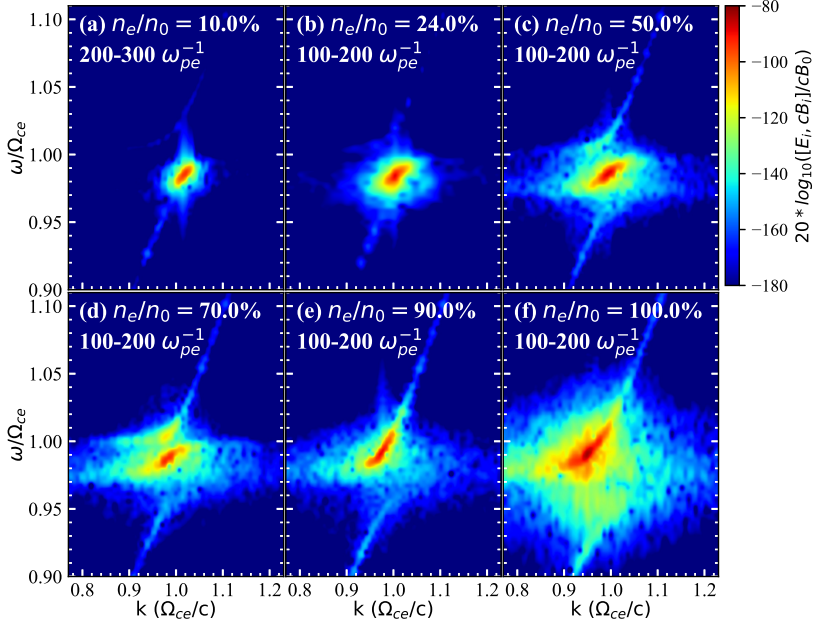


Fig. 5. $\omega - k$ dispersion diagrams of E_y at $\theta_{kB} = 90^\circ$ during the saturation stage for different cases.

the linear kinetic theory ($\sim 0.014 \Omega_{ce}$; see Fig. A.1(e)). According to Fig. 6(g–h), the amplified X-mode waves are linearly polarized with comparable LH and RH intensities.

With the linear kinetic theory (see Section A.3), for the case with $n_e/n_0 = 90\%$, the growth rate of the X mode is 0. This is inconsistent with the corresponding PIC simulation presented above. This can be explained by the evolution of the VDFs (Fig. 4(d)). Almost all of the cool

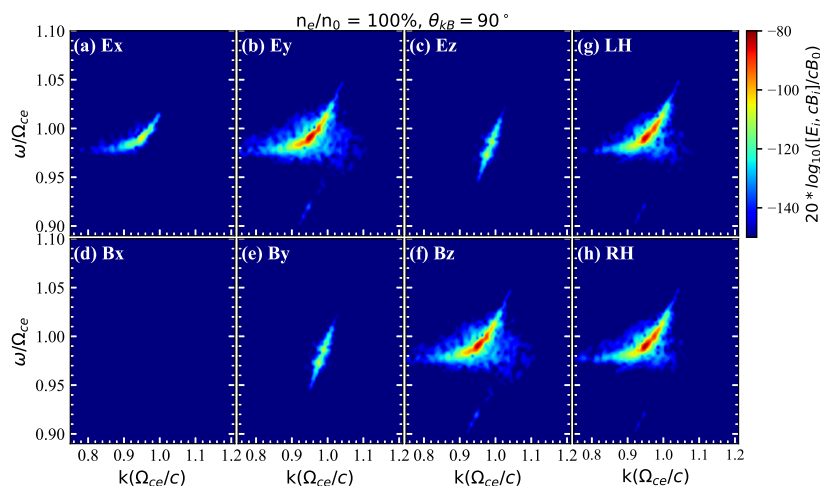


Fig. 6. Wave dispersion diagrams of the six field components (a–f) and the separated LH and RH components (g–h) with $n_e/n_0 = 100\%$ and $\theta_{kB} = 90^\circ$ during $[100, 200] \omega_{pe}^{-1}$.

electrons are energized in the simulation within the first $50 \omega_{pe}^{-1}$, and their VDFs overlap with the hot component. This makes it difficult to distinguish the two components in the phase space, leading to an equivalent case with $n_e/n_0 = 100\%$. This explains why the simulation with $n_e/n_0 = 90\%$ is in line with that of $n_e/n_0 = 100\%$. In other cases with less energetic electrons, the two components of the VDF are still separated until the end of the simulation, and the X mode cannot grow. Further discussion is provided in the following section.

4. Conclusion and discussion

The present study investigates the excitation of the R and X modes based on the in situ observation of SKR sources reported by Menietti et al. (2011). Both PIC simulations and linear theory analysis were performed, and the results are in line with each other. With the given set of parameters, the trapped R mode is amplified as the dominant mode, while the escaping X mode can not grow. The growth rate of the R mode increases with a n_e/n_0 of 10%–70%. The X-mode emissions can only be amplified if the electrons are dominated by hot components ($n_e/n_0 = 90\%$ and 100%) with the cut-off frequency less than Ω_{ce} and the growth rate $\sim 0.018 \Omega_{ce}$. According to our PIC simulations, both the X and R modes can be characterized with similar frequencies ($\sim \Omega_{ce}$), polarization (linearly polarized in E_y), growth rates ($10^{-2} \Omega_{ce}$), and energy conversion rates (1%–3%). The properties can be well explained using the linear kinetic theory.

As the kinetic theory suggests, the X mode can be amplified only with $n_e/n_0 = 100\%$. In other cases with $0 < n_e/n_0 \leq 90\%$, the R mode is the most unstable and the X mode cannot grow. In our simulation with $n_e/n_0 = 90\%$, we observed significant declines of wave energies after the linear stage, with the cold electrons significantly accelerated at $50 \omega_{pe}^{-1}$. We propose a multi-step process to explain the X-mode excitation in this case (and its inconsistency with the linear theory): the R-mode waves are first amplified via ECMI, then interact strongly with the cool electrons and become damped soon via the gyro-resonant absorption. This results in the bulk acceleration of the minor

cool electrons, which then become the “hot” component. This leads to an effective “ $n_e/n_0 = 100\%$ ” case, and thus the strong coupling of the R and X modes and the strong excitation of the X mode. This means that the non-escaping R mode plays a crucial role in the dynamic evolution of electron VDFs and the excitation of the X mode.

However, with the actual measured parameters, we obtained significant excitation of the trapped R mode rather than the escaping X-mode radiation. This does not explain SKR observed from a distance. We propose two possibilities to explain this problem:

1. The measured electron VDFs are not the direct driver of ECMI due to the poor resolution. The CAPS/ELS instrument measures the electrons of different pitch angles using eight detectors, which rotate for approximately 3 min to cover 2π sr of the sky. The temporal resolution is much larger than the timescales of the wave growth ($\sim 100\omega_{pe}^{-1}$). It is hard to measure electrons right before the excitation of ECMI since the VDFs diffuse rapidly at a timescale of 50–100 ω_{pe}^{-1} . Therefore, the ECMI of SKRs may not be induced by the measured electron VDFs.

2. The in situ observation cannot distinguish the R and X modes in the source region. According to our simulations and the linear theory analysis, both the R and X modes are identified as transverse electromagnetic waves with $\omega \sim \Omega_{ce}$, linearly polarized in E_y . These properties are consistent with the observed SKR emissions. With the Cassini in situ measurements of the electric field only, it is difficult to distinguish the two wave modes. In other words, it is possible that the enhancement of the fluctuating electric fields observed by Cassini near or within the sources is actually the trapped R mode, rather than the generally believed escaping X mode.

Saturn’s kilometric radiation has long been considered to be the analogy of the AKR from the geo-magnetosphere. Similar problems were present when applying the ECMI mechanism to AKRs. It is believed that AKRs are generated from low-density cavities with no cold electron population. According to the PIC simulations of the finite source cavity (Pritchett 1986; Pritchett & Winglee 1989; Pritchett et al. 2002), the generated X-mode radiations could escape from the cavities via mode conversion at the boundaries. Although the presence of such cavity structures has not been conclusively identified in SKR sources, this could be a possible explanation for SKR.

In the present simulations, we employed periodical boundary conditions to model the excitation of the wave modes, assuming the electrons are uniformly distributed in a large spatial scale. No replenishment of the electron free energy was included in this model. We will conduct simulations with various setups of the source configurations to examine their effect on the generation process of SKR .

The ECMI growth rates of the X and Z modes in SKR sources have been studied by Mutel et al. (2010) and Menietti et al. (2011). As we pointed out in Section 1, previous studies employed over-simplified dispersion relations with inappropriate assumptions and did not consider the R mode. In this paper, we performed PIC simulations to study the excitation of the three extraordinary modes (R, X, and Z), focusing mainly on the R mode and its effect on the excitation of the X mode. We

also performed linear analysis of the plasma kinetic theory to obtain the dispersion relations and wave growths. The results are in agreement with the PIC simulations.

The R mode is dominant in most cases with both the cold and hot electrons, reaching energies of $\sim 0.03 E_{k0}$. This mode is trapped between plasma layers delimited by the two electron gyro-frequencies (Ω_{ce}/γ , Ω_{ce}), yet it may be converted to escaping emissions when propagating in inhomogeneous plasmas. In addition, the R mode can be absorbed by electrons, leading to the acceleration and heating of plasmas, which, in turn, can modify the dispersion relations. Further simulations should investigate the heating and acceleration process due to the R mode and its coupling with the escaping X mode.

Acknowledgements. This study is supported by NSFC grants (11790303 (11790300), 12203031, and 12103029), the China Postdoctoral Science Foundation (2022TQ0189), and the Natural Science Foundation of Shandong Province (ZR2021QA033). We thank the National Supercomputer Centers in Tianjin and the Beijing Super Cloud Computing Center (BSCC, URL: <http://www.blsc.cn/>) for providing HPC resources, and LANL for the open-source VPIC code.

References

- Bingham, R., Speirs, D. C., Kellett, B. J., et al. 2013, *Space Sci. Rev.*, 178, 695
- Bowers, K. J., Albright, B. J., Yin, L., Bergen, B., & Kwan, T. J. T. 2008, *Physics of Plasmas*, 15, 055703
- Bowers, K. J., Albright, B. J., Yin, L., et al. 2009, in *Journal of Physics Conference Series*, Vol. 180, *Journal of Physics Conference Series*, 012055
- Dory, R. A., Guest, G. E., & Harris, E. G. 1965, *Phys. Rev. Lett.*, 14, 131
- Gurnett, D. A., Kurth, W. S., Kirchner, D. L., et al. 2004, *Space Sci. Rev.*, 114, 395
- Jackman, C. M. 2011, in *Planetary, Solar and Heliospheric Radio Emissions (PRE VII)*, ed. H. O. Rucker, W. S. Kurth, P. Louarn, & G. Fischer, 1–12
- Kaiser, M. L., Desch, M. D., & Lecacheux, A. 1981, *Nature*, 292, 731
- Kaiser, M. L., Desch, M. D., Warwick, J. W., & Pearce, J. B. 1980, *Science*, 209, 1238
- Kimura, T., Lamy, L., Tao, C., et al. 2013, *Journal of Geophysical Research (Space Physics)*, 118, 7019
- Kurth, W. S., Gurnett, D. A., Clarke, J. T., et al. 2005, *Nature*, 433, 722
- Kurth, W. S., Gurnett, D. A., Menietti, J. D., et al. 2011, in *Planetary, Solar and Heliospheric Radio Emissions (PRE VII)*, ed. H. O. Rucker, W. S. Kurth, P. Louarn, & G. Fischer, 75–85
- Lamy, L., Cecconi, B., Prangé, R., et al. 2009, *Journal of Geophysical Research (Space Physics)*, 114, A10212
- Lamy, L., Cecconi, B., Zarka, P., et al. 2011, *Journal of Geophysical Research (Space Physics)*, 116, A04212
- Lamy, L., Schippers, P., Zarka, P., et al. 2010, *Geophys. Res. Lett.*, 37, L12104
- Lamy, L., Zarka, P., Cecconi, B., et al. 2008, *Journal of Geophysical Research (Space Physics)*, 113, A07201
- Lamy, L., Zarka, P., Cecconi, B., et al. 2018, *Science*, 362, aat2027
- Linder, D. R., Coates, A. J., Woodliffe, R. D., et al. 1998, *Geophysical Monograph Series*, 102, 257
- Menietti, J. D., Mutel, R. L., Schippers, P., et al. 2011, *Journal of Geophysical Research (Space Physics)*, 116, A12222
- Mutel, R. L., Menietti, J. D., Gurnett, D. A., et al. 2010, *Geophys. Res. Lett.*, 37, L19105
- Mutel, R. L., Peterson, W. M., Jaeger, T. R., & Scudder, J. D. 2007, *Journal of Geophysical Research (Space Physics)*, 112, A07211
- Ning, H., Chen, Y., Ni, S., et al. 2021a, *A&A*, 651, A118
- Ning, H., Chen, Y., Ni, S., et al. 2021b, *ApJ*, 920, L40
- Pritchett, P. L. 1984a, *Geophys. Res. Lett.*, 11, 143
- Pritchett, P. L. 1984b, *J. Geophys. Res.*, 89, 8957
- Pritchett, P. L. 1986, *J. Geophys. Res.*, 91, 13569
- Pritchett, P. L., Strangeway, R. J., Ergun, R. E., & Carlson, C. W. 2002, *Journal of Geophysical Research (Space Physics)*, 107, 1437

- Pritchett, P. L. & Winglee, R. M. 1989, *J. Geophys. Res.*, 94, 129
- Robinson, P. A. 1986, *Journal of Plasma Physics*, 35, 187
- Schippers, P., Arridge, C. S., Menietti, J. D., et al. 2011, *Journal of Geophysical Research (Space Physics)*, 116, A05203
- Strangeway, R. J. 1985, *J. Geophys. Res.*, 90, 9675
- Strangeway, R. J. 1986, *J. Geophys. Res.*, 91, 3152
- Treumann, R. A. 2006, *A&A Rev.*, 13, 229
- Winglee, R. M. 1983, *Plasma Physics*, 25, 217
- Winglee, R. M. 1985, *ApJ*, 291, 160
- Wu, C. S. 1985, *Space Sci. Rev.*, 41, 215
- Wu, C. S. & Lee, L. C. 1979, *ApJ*, 230, 621
- Young, D. T., Berthelier, J. J., Blanc, M., et al. 2004, *Space Sci. Rev.*, 114, 1

Appendix A: Linear analysis of plasma kinetic theory

A.1. Dispersion tensor

We followed Pritchett (1984b) to derive the dielectric tensors of plasmas with the VDF given by the δ function (Eq. (3)). For perpendicular propagating waves, the elements of plasma dispersion tensors were simplified as

$$\begin{aligned}
S_{xx} &= 1 - r' \frac{\omega_{pe}^2}{\omega^2 - 1} - r \sum_{n=-\infty}^{\infty} \frac{n^2 \omega_{pe}^2}{\xi^2 \omega b} \left(2\xi J_n J_n' - G_r \frac{\omega J_n^2}{b} \right) \\
S_{xy} &= ir' \frac{\omega_{pe}^2}{(\omega^2 - 1)\omega} \\
&\quad + ir \sum_{n=-\infty}^{\infty} \frac{n \omega_{pe}^2}{\omega \xi b} \left[J_n J_n' + \xi (J_n J_n'' + J_n'^2) - G_r \frac{\omega J_n J_n'}{b} \right] = -S_{yx} \\
S_{yy} &= 1 - \frac{k^2 c^2}{\omega^2} - r' \frac{\omega_{pe}^2}{\omega^2 - 1} \\
&\quad - r \sum_{n=-\infty}^{\infty} \frac{\omega_{pe}^2}{\omega b} \left[2J_n'^2 + 2\xi J_n' J_n'' - G_r \frac{\omega J_n'^2}{b} \right] \\
S_{xz} &= S_{zx} = S_{yz} = S_{zy} = 0 \\
S_{zz} &= 1 - \frac{k^2 c^2}{\omega^2} - r' \frac{\omega_{pe}^2}{\omega^2} - r \frac{\omega_{pe}^2}{\gamma_r \omega^2}
\end{aligned} \tag{A.1}$$

where $r = n_e/n_0$, $\xi = ku_r/\Omega_{ce}$, $r' = 1 - r$, $G_r = \gamma_r - 1/\gamma_r$, $\gamma_r = (1 + u_r^2/c^2)^{1/2}$, $b = \gamma_r \omega - n\Omega_{ce}$, and $J_n(\xi)$ refers to the usual Bessel function of order n .

The following equation was solved to obtain both the frequency and growth rate of each extraordinary mode (X, Z, or R):

$$S_{xx}S_{yy} - S_{xy}S_{yx} = 0. \tag{A.2}$$

A.2. ECMI of X and R with $n_e/n_0 = 24\%$

To understand the PIC simulations, we first conducted linear theory analysis with the parameters of SKR sources reported by Menietti et al. (2011). We set $u_r = 0.18 c$, $\gamma_r = 1.016$, $n_e/n_0 = 24\%$, and $\omega_{pe}/\Omega_{ce} = 0.046$.

With a given k , we obtained four sets of complex roots $\omega = \omega_r + i\Gamma$ of Eq. (A.2), representing different branches of the wave modes (see Fig. A.1(a–b)). The dispersion curves of the X mode lie in the range of $\omega_r > \Omega_{ce}$ with a zero growth rate. The slow branch of the extraordinary mode (Z) is below Ω_{ce}/γ_r . Within the range of $\Omega_{ce}/\gamma_r < \omega_r < \Omega_{ce}$ and $k \lesssim \Omega_{ce}/c$, there exist two conjugate roots of the R mode (R1 and R2). The maximum absolute value of their growth rates is $0.006 \Omega_{ce}$. With increasing k ($> \Omega_{ce}/c$), R1 and R2 are decoupled and approach their respective resonant frequency, that is, $\sim \Omega_{ce}$ and Ω_{ce}/γ_r .

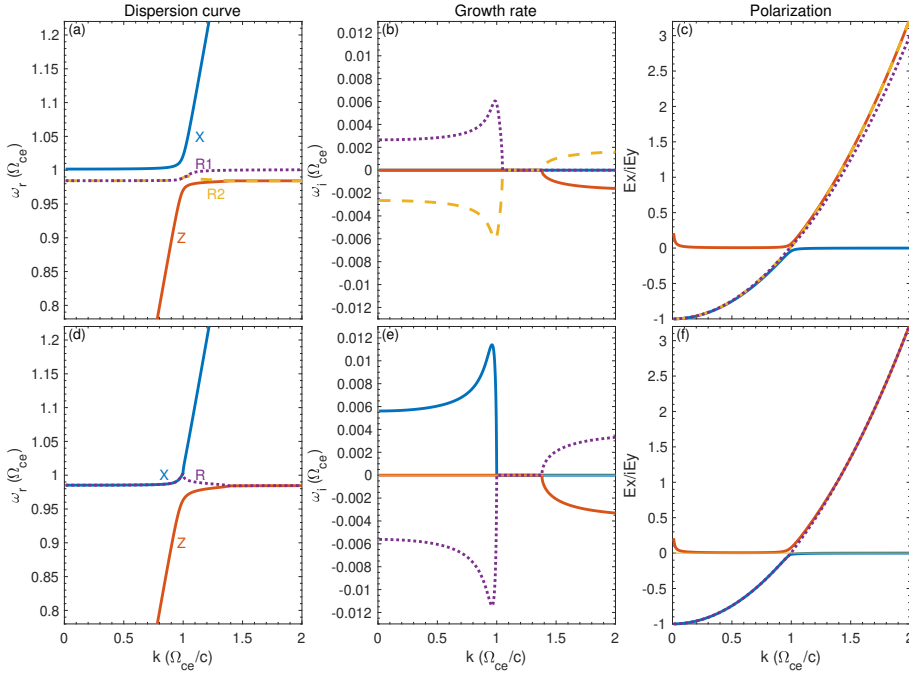


Fig. A.1. Dispersion relation (a, d) and growth rates (b, e) of the extraordinary wave modes according to the kinetic linear theory, with $n_e/n_0 = 24\%$ (upper panels) and 100% (lower panels). The blue and red lines refer to the X and Z modes; the purple and yellow lines refer to the two branches of the relativistic modes (R1 and R2). Panels (c) and (f) present the corresponding intensity ratio of E_x/iE_y for each mode.

The perpendicular-propagating extraordinary waves are mainly carried by E_x and E_y . The polarization was determined by

$$\frac{E_x}{E_y} = -\frac{\varsigma_{xy}}{\varsigma_{xx}}. \quad (\text{A.3})$$

Figure A.1(c) displays the variations in E_x/iE_y with k for each extraordinary mode. With increasing k , E_x/iE_y rises from -1 to 0 for the X mode and from 0 to infinity for the Z mode. The E_x/iE_y of R coincides with that of the X mode, with $k < \Omega_{ce}/c$, and with that of the Z mode, with $k > \Omega_{ce}/c$.

With $n_e/n_0 = 24\%$, R is the most unstable mode, with the highest growth rate at $k \sim \Omega_{ce}/c$; where the three modes are basically linearly polarized with $E_x/iE_y \sim 0$, the X mode cannot be amplified via the ECMI process.

A.3. Parameter studies on n_e/n_0 , ω_{pe}/Ω_{ce} , and u_r

We varied n_e/n_0 from 0 to 100% , keeping the other parameters fixed (Fig. A.2). With $n_e/n_0 = 0$, we obtained the magnetoionic cold-plasma dispersion relation with two branches (X and Z), with no instability.

With $n_e/n_0 > 0$, we obtained conjugate pairs of solutions for the R1, R2, and Z modes, and only those with positive growth rates are presented. The unstable R1 and R2 modes appear within $\Omega_{ce}/\gamma < \omega < \Omega_{ce}$ and their growth rates rise with n_e/n_0 . With a higher abundance of energetic electrons, the X mode has a lower cutoff (ω_X) and its dispersion curve becomes closer to that of the R mode. The X mode is always stable with $\omega_X > \Omega_{ce}$ if $n_e/n_0 < 100\%$.

With $n_e/n_0 = 100\%$, the dispersion curve of the R and X modes merge together, with the cutoff $\omega_X < \Omega_{ce}$. In this case, the X mode can be amplified via ECMI with the highest growth rate, $\sim 0.011 \Omega_{ce}$. As Figure A.1(d–f) shows, the X mode is linearly polarized in E_y ($E_x/iE_y \sim 0$) with $k \gtrsim \Omega_{ce}/c$, and has the highest growth rate at $k \sim \Omega_{ce}/c$. In summary, the linear theory suggests that the R mode is unstable if both cold and hot components are present, while the X mode can only be amplified with $n_e/n_0 = 100\%$.

We further expanded the parameter study by varying ω_{pe}/Ω_{ce} and u_r while fixing $n_e/n_0 (=24\%)$. We find that the R mode is always dominant. With increasing ω_{pe}/Ω_{ce} (from 0.01 to 0.25) or u_r (from 0.05 to 0.3 c), the dispersion curves of the R mode appear in a broader range of frequencies with increasing growth rates.

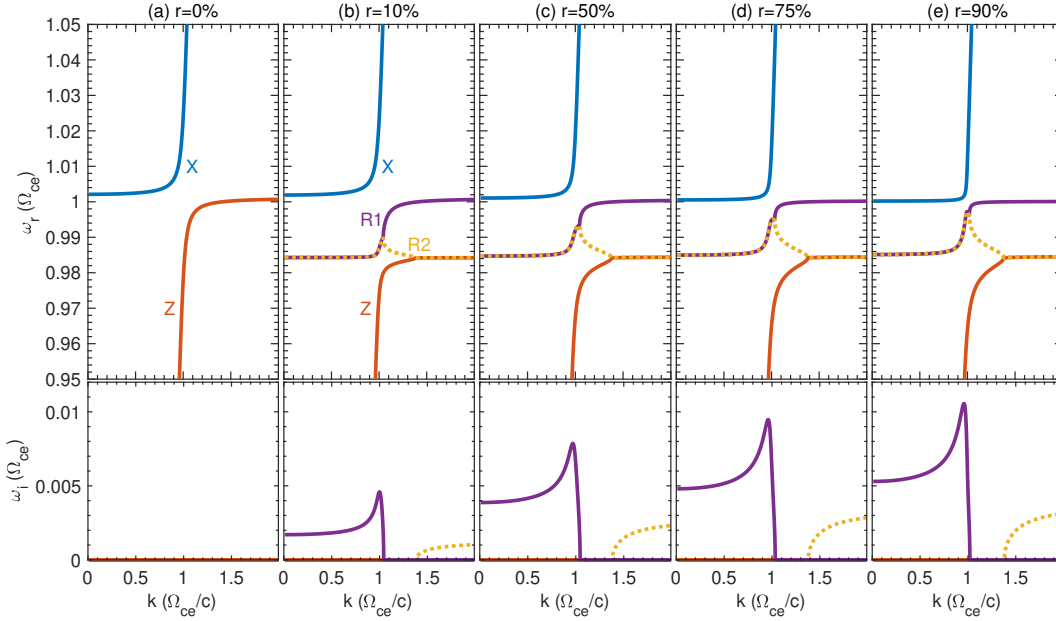


Fig. A.2. Dispersion relation (upper panels) and growth rates (lower panels) of the extraordinary wave modes (X, R1, R2, and Z) with varying n_e/n_0 .